PHYSICAL REVIEW B **99**, 245205 (2019)

Defects and mechanical properties in weakly damaged Si ion implanted GaAs

S. Creutzburg,[1,2,3,*] E. Schmidt,[1] P. Kutza,[1] R. Loetzsch,[4,5] I. Uschmann,[4,5] A. Undisz,[6] M. Rettenmayr,[6] F. Gala,[7] G. Zollo,[7] A. Boulle,[8] A. Debelle,[9] and E. Wendler[1,†]

[1]*Institut für Festkörperphysik, Friedrich-Schiller-Universität Jena, Max-Wien-Platz 1, 07743 Jena, Germany*
[2]*Institut für Ionenstrahlphysik und Materialforschung, Helmholtz-Zentrum Dresden-Rossendorf,*
Bautzner Landstrasse 400, 01328 Dresden, Germany
[3]*Technische Universität Dresden, 01069 Dresden, Germany*
[4]*Institut für Optik und Quantenelektronik, Friedrich-Schiller-Universität Jena, Max-Wien-Platz 1, 07743 Jena, Germany*
[5]*Helmholtz-Institut Jena, Fröbelstieg 3, 07743 Jena, Germany*
[6]*Otto-Schott-Institut für Materialforschung (OSIM), Friedrich-Schiller-Universität Jena, Löbdergraben 32, 07743 Jena, Germany*
[7]*Dipartimento di Scienze di Base e Applicate per l'Ingegneria, Università di Roma "La Sapienza",*
Via A. Scarpa 14-16, 00161 Rome, Italy
[8]*Institut de Recherche sur les Céramiques, CNRS UMR 7315, Centre Européen de la Céramique, 12 rue Atlantis, 87068 Limoges, France*
[9]*Centre de Sciences Nucléaires et de Sciences de la Matière, Université Paris-Sud, CNRS/IN2P3,*
Université Paris-Saclay, 91405 Orsay, France

(Received 29 March 2019; revised manuscript received 5 June 2019; published 24 June 2019)

Damage formation is investigated in GaAs implanted with 1 MeV Si ions to ion fluences from 3×10^{12} to 5×10^{15} cm^{-2} at room temperature. Under the conditions applied, amorphization of the implanted layers does not occur. The weakly damaged layers are studied by applying different experimental techniques including Rutherford backscattering spectrometry in channeling configuration, x-ray diffraction, *in situ* curvature measurement, optical subgap spectroscopy, and transmission electron microscopy. The results are evaluated and quantitatively connected with each other. Damage formation is described as a function of the ion fluence using a common defect evolution model. Point defects and defect clusters have to be taken into account in the ion fluence range of main interest up to 2×10^{15} cm^{-2}. Point defects contribute by a factor of about 8 more to both perpendicular strain and in-plane stress than defect clusters. When the concentration of point defects or the induced strain reaches a critical value, defect clusters form, which ensures that no further increase of perpendicular strain occurs. This reveals a clear driving force for cluster formation. The microstructure of the defect clusters cannot be determined from the results. As_3Ga_2 interstitial clusters are supposed. A remarkable decrease of the shear modulus of the implanted layers below the value of pristine GaAs by $\approx -35\%$ is observed. Surprisingly, the change of shear modulus already sets in at a very low damage level of a few percent.

DOI: 10.1103/PhysRevB.99.245205

I. INTRODUCTION

Ion implantation is a well-established method in semiconductor technology, but it is also applied for the modification of the refractive index of optical crystals (see, e.g., [1,2]). The process of ion implantation is inherently connected with the formation of radiation damage. For many applications, the radiation damage needs to be annealed and the most efficient annealing conditions may depend on the kind and concentration of damage produced by the implantation process. For this reason, any practical application of ion implantation requires a certain knowledge about the relation between implantation conditions and defects remaining after implantation in the respective material. This has triggered a continuous research of ion-beam-induced effects in various crystalline materials since many years (for a more recent overview, see [2] and references therein). Additionally, ion implantation acts as a tool for producing special states in a solid for further investigations. Because it is a nonequilibrium process, foreign atoms can be introduced into a solid with concentrations exceeding the corresponding solid solubility limit, which is important for ion-beam-induced formation of nanocrystals (see, e.g. [3] and Chap. 4 in [2], and references therein). Ion implantation produces amorphous layers in many materials at sufficiently low temperatures, which exhibit a higher degree of disorder than amorphous layers grown for instance by chemical vapor deposition [4–6]. And, finally, a maximum concentration of point defects and point-defect complexes can be introduced into crystals by choosing appropriate implantation conditions [7].

In this paper, weakly damaged gallium arsenide (GaAs) is investigated which is produced by implantation of 1 MeV silicon (Si) ions at room temperature. Next to silicon and indium phosphide, GaAs is the most important semiconductor material, the behavior of which during ion irradiation has been studied since more than 40 years (see Chaps. 5 and 6 in [2] and references therein). The process of ion-beam-induced amorphization is rather well understood on the basis

---

[*] s.creutzburg@hzdr.de
[†] elke.wendler@uni-jena.de

of the phenomenological model of critical temperatures (see Chaps. 5 and 6 in [2]). In contrast to amorphous GaAs, weakly damaged (also called defective crystalline) GaAs can be produced by ion implantation of light ions at temperatures around room temperature or by neutron irradiation. The electron diffraction pattern of such implanted layers agrees with those of pristine GaAs [7]. But, this material is characterized by a tremendous increase of the optical absorption coefficient at photon energies below the fundamental absorption edge [8,9]. For higher wavelengths, the absorption coefficient even exceeds that of amorphous GaAs significantly [10]. In difference to that, the refractive index remains nearly at the value of the substrate, whereas a refractive index increase of about 15% is obtained in case of amorphous GaAs. The exponentially increasing subgap absorption coefficient is usually called the Urbach tail [11]. Such tails also occur in heavily doped GaAs with characteristic or tailing energies of a few tens of meV (see, e.g., [12]). In weakly damaged ion implanted GaAs the tailing energies reach values of a few hundreds of meV [9,10]. Currently, such band tails attract special attention in kesterite crystals [13], which are seen as promising semiconductors for photovoltaics. However, so far no satisfying theory exists for representing both absorption coefficient and refractive index versus photon energy for different defect concentrations in a given material. Therefore, one stimulus of our work is to provide data as a basis for future theoretical developments in this field. Second, our aim is obtaining a more comprehensive picture about the process of defect formation in GaAs during ion implantation in the regime of low damage with special emphasis on mechanical properties such as out-of-plain strain and in-plane stress. In this work, several experimental techniques were applied for investigating one and the same set of samples. This is different from most of previous works in this field, which often used only one method for analysis. Additionally, it should be mentioned that the experimental techniques themselves as well as the data evaluation improved significantly in recent times.

Samples of ⟨100⟩ oriented GaAs were implanted with 1 MeV Si ions to ion fluences between 3×10^{12} and 5×10^{15} cm^{-2}. After introducing the experimental conditions in Sec. II, in Sec. III A the defects are characterized by Rutherford backscattering spectrometry in channeling configuration (RBS/C) and by transmission electron microscopy (TEM). The defect-induced strain and in-plane stress are analyzed in Sec. III B. Section III C presents the subgap optical properties of the weakly damaged GaAs layers. In the discussion in Sec. IV, two main types of defects are identified and their influence on the lattice strain perpendicular to the surface [detected by x-ray diffraction (XRD)] and on the in-plane stress (deduced from the curvature of the sample measured *in situ* during the implantation) is analyzed. A common defect evolution model is applied to elucidate the mechanisms of defect formation as a function of ion fluence. The obtained parameters are discussed. Finally, the point-defect concentration is estimated.

II. EXPERIMENTAL CONDITIONS

Nominally undoped ⟨100⟩ GaAs samples polished on both sides were implanted at room temperature with 1 MeV Si ions. The ion fluence N_I varied between 3×10^{12} and 5×10^{15} cm^{-2}. The ion currrent was kept constant at 25 nA cm^{-2}, corresponding to an ion flux of 1.4×10^{11} s^{-1} cm^{-2}. The implantations were carried out 7° off axis to minimize channeling of the implanted ions.

RBS/C measurements were performed *ex situ* using He ions with energies of 1.4 and 1.8 MeV and a backscattering angle of 170°. For both energies, spectra were recorded at room temperature (RT). Furthermore, the implanted samples were investigated at a lower temperature of 107 K (LT) using He ions of 1.4 MeV energy to determine the mean displacement distance of displaced atoms perpendicular to the ⟨100⟩ axis. The incident He ions generate additional damage during the RBS/C measurements [14]. Therefore, spectra were measured as a function of charge. For each sample, eight spectra were recorded with a constant charge per spectrum. At RT, the yield of the eighth spectrum lies still within the range of statistical uncertainty of the first spectrum. At LT, the yield of the eighth spectrum was clearly higher than that of the first spectrum, which made an extrapolation indispensable. A linear increase of the yield with the number of spectra was found. Thus, the yield of each channel was extrapolated to zero charge for obtaining a spectrum being undisturbed by the analyzing He ions. For damage analysis, the difference in minimum yield given by $\Delta\chi_{\text{min}} = (Y_{\text{al}}^{\text{impl}} - Y_{\text{al}}^{\text{perf}})/Y_{\text{ra}}$ was calculated [$Y_{\text{al}}^{\text{impl}}$, $Y_{\text{al}}^{\text{perf}}$: backscattering yields in aligned direction for the implanted and perfect (i.e., unimplanted) crystal; Y_{ra}: backscattering yield in random direction]. The evaluation of $\Delta\chi_{\text{min}}$ was conducted with DICADA [15–18] based on the discontinuous model of dechanneling [15]. In order to consider thermal vibrations, the Debye temperature was estimated by achieving the best agreement between the measured and the simulated $\chi_{\text{min}}^{\text{perf}} = Y_{\text{al}}^{\text{perf}}/Y_{\text{ra}}$ curve of an unimplanted sample. In case of 107 and 296 K, Debye temperatures of $T_{\text{D}} = (220\pm10)$ and (260 ± 10) K, respectively, were determined, which are in good agreement with values from Breeger *et al.* [19,20]. It was assumed that the thermal vibration amplitude of displaced atoms and of those located at perfect lattice sites is the same. Selected samples were investigated by RBS/C using different energies of the incident He ions (1.4, 1.8, 2.4, and 3.0 MeV) to obtain further information about the present kinds of defects [21].

X-ray double-crystal diffraction measurements were performed *ex situ* in nondispersive geometry. Rocking curves of the (400) reflection were measured using Cu $K\alpha$ radiation ($\lambda = 1.5418$ Å) to investigate the strain perpendicular to the ⟨100⟩ surface. Additionally asymmetrical rocking curves of the (533) reflection were recorded at gracing exit using Ni $K\alpha$ ($\lambda = 1.6599$ Å) to analyze the parallel strain. In order to obtain depth profiles of strain, the rocking curves of the (400) reflection were analyzed in more detail by using RADMAX [22] based on the Takagi-Taupin equations [23–25].

The in-plane stress was investigated by measuring the curvature of a sample *in situ* during the implantation up to an ion fluence of 1.1×10^{15} cm^{-2}. For this experiment, a sample was cut in a rectangular piece with lateral dimensions of $5\times\ 10$ mm^2. This sample was fixed at one side to a target holder in order to provide a freestanding sample which was able to bend during ion irradiation. The radius of curvature was measured from the back side of the sample by means of a scanning laser reflection technique while the sample was implanted at the front side [26–29]. In his pioneering work, EerNisse already stated that strain is very sensitive to low concentrations of lattice defects and a high amount of useful data can be obtained with such a technique in a short time [30].

Optical transmission measurements were carried out *ex situ* in the region below the band-gap energy (0.6 eV $< E_{\mathrm{photon}} <$ 1.3 eV) using a two-beam UV-VIS spectrometer from Varian. The near-edge absorption coefficient was examined, which is highly sensitive to the concentration of point defects [31]. The samples were treated as a two-layer system consisting of the implanted layer and the underlying substrate, both exhibiting the same refractive index. In this case, the absorption coefficient, integrated over the depth of the implanted layer, can be calculated.

Transmission electron microscopy (TEM) was carried out in a JEOL JEM-3010 operated at an accelerating voltage of 300 kV. A lamella of the sample implanted with 2×10^{15} cm^{-2} was prepared using the common focused ion-beam technique.

In order to compare the depth distributions of measured quantities with the number of primary displacements produced by the implanted ions, calculations with SRIM (stopping and ranges of ions in matter) version 2008.04 [32] were performed. The number of primary displacements per ion and unit depth $N^*_{\mathrm{displ}}(z)$ was calculated applying the displacement energies $E_{\mathrm{Ga}} = 8.8$ eV and $E_{\mathrm{As}} = 10.1$ eV [33]. The value in the maximum of the distribution amounts to 2.15/(ion Å). Taking into account the atomic density of GaAs of $N_0 = 4.4 \times 10^{22}$ cm^{-3}, this corresponds to a cross section of $\sigma_{\mathrm{SRIM}} = 4.9 \times 10^{-15}$ cm^2. For a given depth z, the ion fluence N_{I} can be converted to the number of primary displacements per lattice atom (dpa) by $N_{\mathrm{I}} \cdot N^*_{\mathrm{displ}}(z)/N_0$.

III. RESULTS

A. Characterization of defects by RBS/C and TEM

Figure 1(a) shows RBS/C spectra of 1.4 MeV He ions backscattered at RT on GaAs implanted with 1 MeV Si ions to different ion fluences N_I. In case of RBS/C any defects exhibit as displaced lattice atoms which contribute to direct backscattering and dechanneling of the analyzing He ions. The spectra up to a fluence of 2×10^{15} cm^{-2} are characterized by a strong dechanneling. No significant contribution of direct backscattering, i.e., no pronounced damage peaks, are visible. This suggests the existence of distorted crystalline regions induced by point defects and defect clusters. Up to 6×10^{14} cm^{-2} the backscattering yield rises due to the formation of defects. Between 6×10^{14} and 2×10^{15} cm^{-2}, the yield increases rather weakly. A stronger increase of the yield is again observed between 2×10^{15} and 5×10^{15} cm^{-2}. This is most probably caused by the formation of more heavily damaged and/or amorphous regions.

In case of RBS/C spectra as shown in Fig. 1(a), a random displacement of atoms from their original lattice sites cannot automatically be assumed. The mean displacement distance is an unknown quantity which has to be determined. This in turn means that common two-beam approximations cannot be used for the determination of concentration and depth distribution of displaced lattice atoms. We measured the difference in minimum yield $\Delta\chi_{\mathrm{min}}$ at two different temperatures. The data were evaluated applying the DICADA code (see Sec. II). The temperature dependence of $\Delta\chi_{\mathrm{min}}$ is sensitive to the mean distance of displaced atoms from their original lattice site perpendicular to the axis of incidence [16]. A negative temperature dependence means $\Delta\chi_{\mathrm{min}}(107\ \mathrm{K}) > \Delta\chi_{\mathrm{min}}(296\ \mathrm{K})$. It indicates the presence of a high concentration of slightly displaced atoms. A positive temperature dependence with $\Delta\chi_{\mathrm{min}}(107\ \mathrm{K}) < \Delta\chi_{\mathrm{min}}(296\ \mathrm{K})$ points to larger values or a random distribution of the displacement distances.

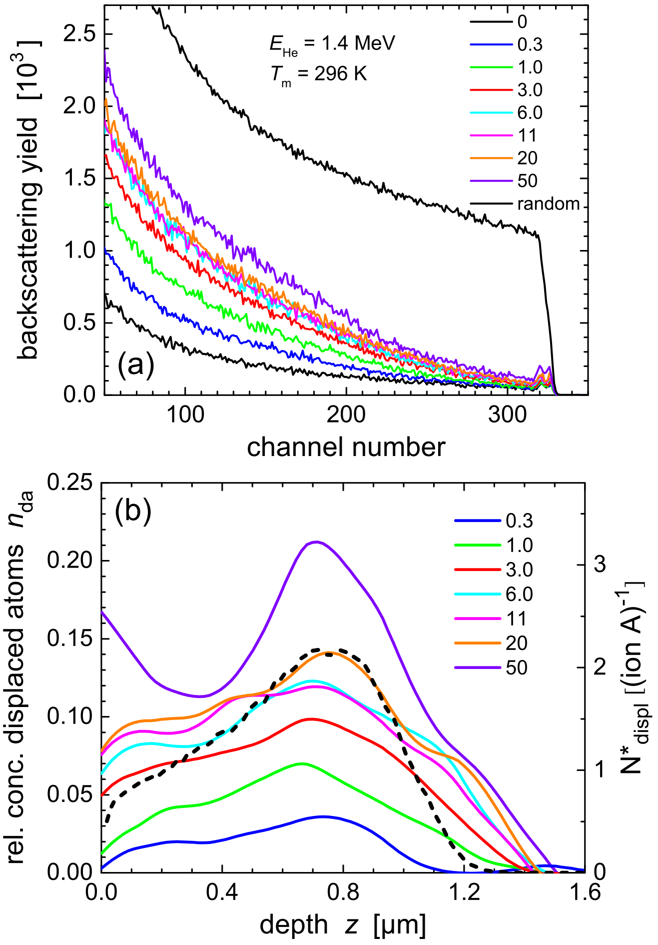

FIG. 1. RBS/C spectra (a) measured at 296 K using He ions of 1.4 MeV energy and (b) relative concentration of displaced lattice atoms versus depth $n_{\mathrm{da}}(z)$, calculated from the spectra in (a) with a displacement distance of 0.51 Å. Ion fluences are given in 10^{14} cm^{-2}. For comparison, the number of primary displacements per ion and unit depth $N^*_{\mathrm{displ}}(z)$, calculated by SRIM, is plotted in (b) as dashed line (left scale).

The procedure for determining the mean displacement distance r_{d} and the depth distribution of the relative concentration of displaced lattice atoms $n_{\mathrm{da}}(z)$ was demonstrated in previous works [34,35]. Here, it was applied to each sample with ion fluences between 3×10^{13} and 5×10^{15} cm^{-2} [see Fig. 1(a)]. In all cases, $\Delta\chi_{\mathrm{min}}$ shows a positive temperature dependence. The evaluation reveals a constant mean displacement distance of (0.51 ± 0.2) Å for all ion fluences. This coincides with results for 2 MeV Se implanted GaAs and ion fluences above 1×10^{12} cm^{-2}, for which $r_d = (0.50 \ldots 0.65)$ Å was obtained [36]. It should be mentioned that in previous works on ion implanted GaAs a negative temperature dependence of $\Delta\chi_{\min}$ was observed, but only for very low ion fluences. This yields a high concentration (of up to 50%) of only slightly displaced lattice atoms ($r_{d1} \approx 0.2$ Å) [34,36–38]. This high concentration and the low displacement distance of displaced lattice atoms was attributed to the preferred occurrence of vacancy, antisite, and/or vacancy-antisite complexes [34]. Additionally, the given values can be understood by a low concentration of isolated point defects, each of them creating its own remarkable local distortion field [36]. With proceeding implantation, the higher defect concentration may cause an overlapping and relative reduction of the distortion field. Already existing point defects may trap mobile interstitial atoms. This transformation of defects can explain the increase of the mean displacement distance up to $r_{d2} \approx 0.65$ Å and the decrease of the concentration of displaced lattice atoms down to a saturation value of about 10% at higher ion fluences [34]. It is hard to predict at which ion fluence such a defect transformation occurs. Especially around RT slight variations of ion flux and/or temperature may lead to a different microstructure of the defects [39–43] and thus to a different temperature dependence of $\Delta\chi_{\min}$. The constant and relatively large displacement distance of $r_d = 0.51$ Å obtained here suggests that a regime was realized for which interstitial atoms were already trapped. Thus, interstitial atoms seem to constitute an important component of point-defect complexes remaining after implantation.

The depth profiles $n_{da}(z)$ for all ion fluences resulting for $r_d = 0.51$ Å are plotted in Fig. 1(b). The depth distribution of the number of primary displacements per ion and unit depth $N^*_{\mathrm{displ}}(z)$ calculated by SRIM is added in Fig. 1(b) for comparison. For all fluences, the depth of maximum defect concentration agrees well with the depth of maximum concentration of primarily displaced atoms as calculated with SRIM. For fluences above 3×10^{13} cm^{-2}, the measurements show displaced atoms at depths larger than that predicted by SRIM. This effect was already observed in previous works [44]. From Fig. 1(b) it can be seen that the concentration n_{da} in the maximum of the distribution increases with increasing ion fluence in a similar way as it was found for 280/325 keV N ion implanted GaAs with $r_{d2} = 0.65$ Å [34,37] and for 2 MeV Se ion implanted GaAs (ion fluences above 1×10^{12} cm^{-2}) [36]. This indicates that the concentration of heavily displaced atoms increases with increasing concentration of defects. Thus, these two quantities are directly related to each other. However, from Fig. 1(b) it can be seen that n_{da} reaches values up to about 0.15, i.e., up to 15%. Point defects in such high concentrations cannot exist in a crystal. Thus, it is obvious that the concentration of displaced lattice atoms is not exactly the concentration of defects. One defect causes more than one displaced lattice atom visible by RBS/C. This will be discussed in more detail in Sec. IV C. However, for simplicity and because a precise, real concentration of defects can be hardly determined, n_{da} is regarded as defect density in the following text.

To obtain further information about the present types of defects, selected samples were measured by means of RBS/C using different energies [21] of the incident He ions (1.4, 1.8, 2.4, and 3.0 MeV) at room temperature. Samples implanted with ion fluences of 1×10^{14} cm^{-2}, 6×10^{14} cm^{-2} and 2×10^{15} cm^{-2} were investigated. In Fig. 2 the difference in minimum yield $\Delta\chi_{\min}$ taken at a depth of 1.0 μm is shown versus the energy E_{He} of incident He ions. The symbols represent the experimental values determined from the measured RBS/C spectra. From the $\Delta\chi_{\min}$ spectra, which were measured at an energy of 1.4 MeV, profiles of displaced atoms were calculated using DICADA assuming uncorrelated displaced lattice atoms with a mean displacement distance of 0.51 Å. Applying these profiles, $\Delta\chi_{\min}$ was calculated for the other He ion energies used of 1.8, 2.4. and 3.0 MeV. The calculated values of $\Delta\chi_{\min}$ at a depth of 1.0 μm are included in Fig. 2 as solid lines. In case of 1×10^{14} cm^{-2} and 6×10^{14} cm^{-2} the calculated values lie within the uncertainty of the measured ones. Hence, we can conclude that uncorrelated displaced atoms mainly contribute to the dechanneling of the analyzing He ions for these fluences. This points to the existence of point defects which are connected with uncorrelated displaced atoms. For 2×10^{15} cm^{-2} the experimental and calculated values match only for 1.8 MeV. For 2.4 and 3.0 MeV, the calculated values are well below the experimental ones. This means that for the GaAs sample implanted to 2×10^{15} cm^{-2} the energy dependence of the difference in minimum yield is not well represented by assuming uncorrelated displaced lattice atoms only. Additional defect structures must have formed that cause a correlated displacement of lattice atoms. Small extended defects or slightly misaligned crystalline regions are possible candidates.

In order to attain details regarding the microstructure of defects, the sample implanted with 2×10^{15} cm^{-2} was

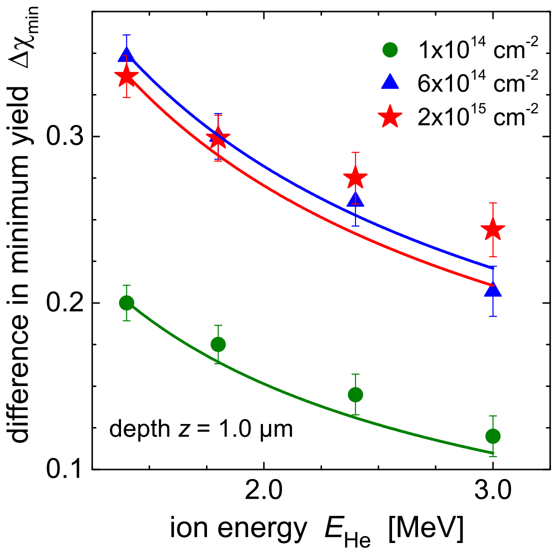

FIG. 2. Difference in minimum yield $\Delta\chi_{\min}$ at a depth of 1.0 μm versus energy E_{He} of incident He ions for selected ion fluences N_I. The experimental values are depicted as symbols. By applying the measured $\Delta\chi_{\min}$ for He ions with energy of 1.4 MeV, profiles of displaced atoms were calculated assuming a displacement distance of 0.51 Å. They serve as input for calculating $\Delta\chi_{\min}$ for the other He-ion energies applied. The thus calculated $\Delta\chi_{\min}$ values at a depth of 1.0 μm are added as solid lines.

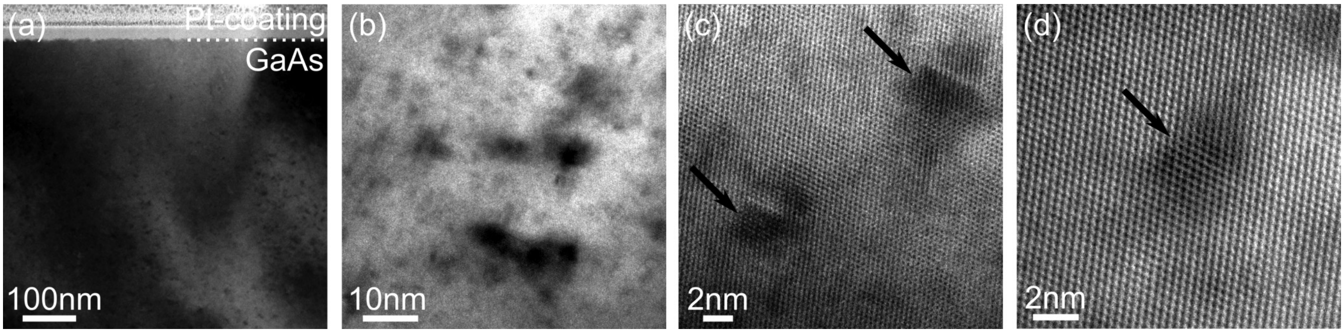

FIG. 3. Cross-sectional TEM images of the GaAs sample implanted with 2×10^{15} cm^{-2}. (a) Overview illustrating the presence of numerous small dark areas (∅ < 20 nm) as a consequence of local strains present in the crystal lattice. (b)–(d) Images with increasing magnification displaying details of the small dark areas (black arrows) up to the atomic level. Images (b)–(d) were recorded at a depth of 200 to 300 nm, representing the optimum regarding sufficiently high defect density and sufficiently low thickness of the lamella to allow for HR-TEM.

investigated by cross-sectional TEM (Fig. 3). Numerous small dark areas (∅ < 20 nm) are observed in the GaAs matrix [Fig. 3(a)]. The number of the dark areas increases with increasing distance from the surface, consistent with the implantation depth of the ions used. Apparently, the dark contrasts are a consequence of local strains due to implantation-induced defect clusters. This finding and the conclusion agree with that of previous TEM investigations on similarly damaged GaAs layers produced by 280 keV N ions [7]. In Fig. 3(a), higher-dimensional crystal defects, e.g., dislocations, are not visible in the respective areas, again in accord with results for 325 keV N ion implanted GaAs [37]. At higher magnifications [Figs. 3(b)–3(d)] it becomes obvious that the lattice planes of the GaAs matrix proceed through the defect clusters. However, due to local strains a mild shift of the local orientation is indicated by locally different visibility of atom columns [Fig. 3(d)]. This finding is consistent with results of the energy-dependent RBS/C analysis.

B. Defect-induced strain and in-plane stress

Rocking curves of the (400) reflection were recorded to investigate the strain perpendicular to the surface. The measured curves are depicted in Fig. 4(a). Interference structures arise on the low-angle side of the GaAs substrate peak indicating an increase of the interplanar spacing in the implanted layer perpendicular to the surface. This means an expansion of the lattice. Hence, it can be concluded, in coincidence with the RBS/C results, that the defects are preferably interstitial-like [45]. It should be noted that the presence of arsenic antisites can also lead to an expansion of the lattice [46]. The perpendicular strain $\epsilon_\perp$ is defined by

$$\epsilon_\perp = \frac{a_{\perp,\text{layer}} - a_{\text{substrate}}}{a_{\text{substrate}}}, \tag{1}$$

where $a_{\perp,\text{layer}}$ is the lattice parameter of the implanted layer perpendicular to the surface and $a_{\text{substrate}}$ is the lattice parameter of the substrate. The spacing of the fringes corresponds to the width of the strained region for a given strain level [47,48].

In order to obtain strain depth profiles rocking curves of the (400) reflection were simulated and fitted to the measured ones as described in Sec. II. Strain profiles with different depths of maximum strain can lead to the same rocking curves [47]. Therefore, the profiles were simulated under the assumption that the depth of maximum strain is close to the depth of maximum number of displacements. This assumption is justified by the fact that the defect distribution determined with RBS/C has its maximum at the same depth. Rocking curves were recorded with a wide open detector also collecting contributions of diffuse scattering, which is not considered in RADMAX and causes an angle-dependent background. Thus, the heights of the amplitudes may be impacted by diffuse scattering leading to wrong Debye-Waller profiles.

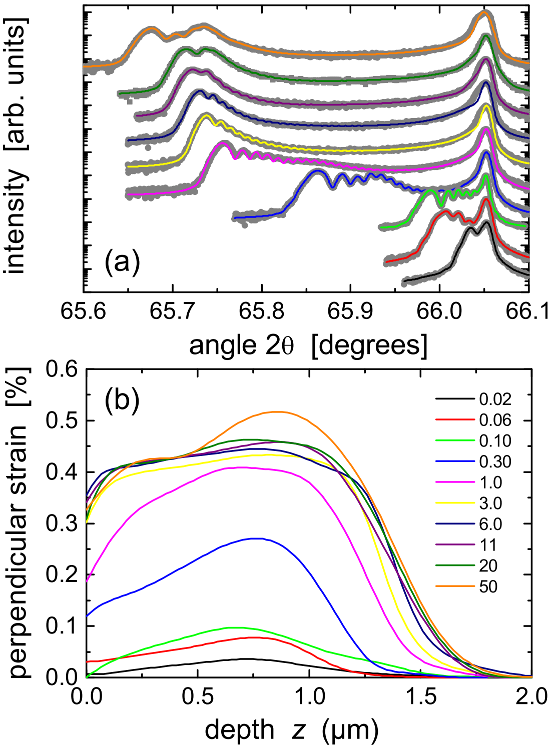

FIG. 4. Rocking curves of the (400) reflection (a), which were measured using Cu $K\alpha$ radiation, and (b) depth profiles of perpendicular strain $\epsilon_\perp(z)$, obtained by fitting the spectra in (a). Ion fluences are given in 10^{14} cm^{-2}. In (a) the experimental data are given as gray dots. The solid lines are best fits of the spectra yielding the profiles shown in (b).

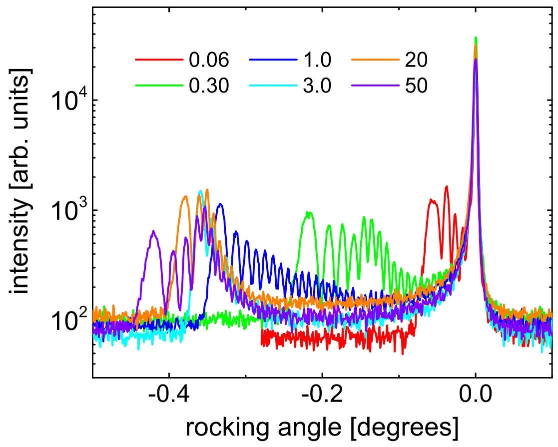

FIG. 5. Rocking curves of the (533) reflection, which were measured at high-angle incidence using Ni $K\alpha$ radiation. The rocking angle denotes the angle difference related to the Bragg peak of the GaAs substrate. Ion fluences are given in 10^{14} cm^{-2}.

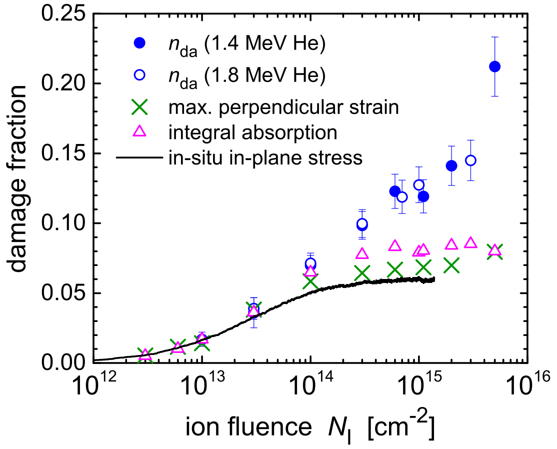

FIG. 6. Damage fraction determined by different experimental techniques versus ion fluence N_I. n_da is the maximum relative concentration of displaced lattice atoms from the RBS/C analysis. The percentage of maximum perpendicular strain $\epsilon_\perp$, the integral optical absorption coefficient Kd, and the integrated in-plane stress S are obtained by dividing the plotted numbers by 0.15, 0.015, and 2.6×10^{-4}, respectively.

Formerly, it was observed that changes of the strain profiles affect the position of the peaks whereas the Debye-Waller profile determines the heights of the amplitudes [49]. Hence, it was ensured that the peak positions of the simulated and of the measured curves match. The Debye-Waller profiles were modified to obtain the best agreement of the intensities. Figure 4(a) depicts the measured and simulated rocking curves of the (400) reflection. An excellent agreement is obtained. The resulting depth profiles $\epsilon_\perp(z)$ are plotted in Fig. 4(b). The shape of these strain profiles is in good agreement with that of the defect profiles determined by RBS/C [see Fig. 1(b)]. The close correlation between displaced lattice atoms and strain becomes especially obvious when plotting the maximum values $\epsilon_\perp$ against n_da which yields a uniform curve [cf. Figs. 1(b) and 4(b)].

The profiles of strain broaden toward the surface and toward depths once the saturation level of perpendicular strain is reached in the maximum [see Fig. 4(b)]. A rather homogenously strained layer is produced for ion fluence above 3×10^{14} cm^{-2}. The saturation value of the perpendicular strain amounts to about 0.4% in this range. This value is in good agreement with saturation values already observed in case of GaAs implanted with other ion species or ion energies [50–53]. Only at 5×10^{15} cm^{-2} the shape of the profiles changes and a further peak on top of the plateau appears. This suggests the occurrence of more heavily damaged and/or amorphous regions in coincidence with the interpretation of the RBS/C spectra.

The parallel strain in the implanted layer is defined in the same way as the perpendicular one [see Eq. (1)]. It is estimated from asymmetrical rocking curves of the (533) reflection recorded at gracing exit with Ni $K\alpha$ radiation (see Fig. 5) following the procedure given in Refs. [54–56]. The obtained values of the parallel strain are slightly negative. As found for the maximum perpendicular strain $\epsilon_{\perp,\max}$, the parallel strain develops with ion fluence and saturates at about 1×10^{14} cm^{-2}. The values lie between $(-0.003 \pm 0.003)\%$ (for 3×10^{12} cm^{-2}) and $(-0.036 \pm 0.006)\%$ (for 5×10^{15} cm^{-2}). Such small negative values for the parallel strain were already determined in previous works [51,54]. The parallel strain is more than one order of magnitude smaller than the maximum perpendicular strain and is therefore neglected in further considerations.

The buildup of in-plane stress was deduced from the radius of curvature R of an implanted sample measured *in situ* during the irradiation (see Sec. II). Based on the assumption that the thickness of the irradiated surface layer t_imp is much smaller than that of the undamaged substrate t_sub (thin-film analysis which is well fulfilled in our case), the integrated in-plane stress S of the sample is related to R according to the Stoney equation [57]

$$S = \int_0^{t_\mathrm{imp}} \sigma_\parallel(z) dz = \frac{Y_\mathrm{c} t_\mathrm{sub}^2}{6R}. \tag{2}$$

Herein, $\sigma_\parallel(z)$ is the local in-plane stress and Y_c denotes the biaxial Young modulus of the undamaged (crystalline) substrate with $Y_\mathrm{c} = 8.59 \times 10^{10}\,\mathrm{N/m^2}$ for GaAs [58]. The evolution of S with increasing ion fluence N_I is included in Fig. 6. This figure summarizes fluence dependencies for the various quantities measured (see discussion below). It is found that in-plane stress builds up up to an ion fluence of 1.1×10^{15} cm^{-2}, which is the highest value applied in this experiment. The slope of $S(N_\mathrm{I})$ is rather high up to about 1×10^{14} cm^{-2} and becomes significantly weaker for higher ion fluences. Previously, the in-plane stress S was studied for ion implanted silicon [27,30] and germanium [28]. In these works, a significant stress reduction was observed beginning at a certain ion fluence. This decrease of S could be attributed to amorphization of the implanted layer. We confirmed this decrease of stress also for ion-beam-induced amorphization of GaAs by performing the *in situ* curvature measurement during 1 MeV Si ion implantation at a temperature of about 140 K (not shown). For the defect state produced by 1 MeV Si ion implantation in GaAs at RT, which is the scope of this paper, no decrease of the in-plane stress was observed. Therefore, it can be concluded that up to a fluence of about 1.1×10^{15} cm^{-2} no amorphous GaAs is to be expected. Finally, it should be mentioned that during the curvature measurement at RT, no ion-beam on/off effects (see, e.g., [28]) were observed. After switching the beam off, the curvature remained constant.

C. Optical subgap properties

The integrated absorption coefficient $Kd = \int_0^{t_{\rm imp}} K(z)dz$ of the implanted layer was determined from the transmission spectra as described in Sec. II with K being the absorption coefficient. Kd reveals an exponential dependence on the photon energy $\hbar w$ below the band-gap energy. This effect was already investigated in previous works [7,9,10,44]. The integrated absorption coefficient was fitted according to $Kd \propto \exp(\hbar w/E_1)$. The presence of arbitrarily distributed charged impurities is connected with a perturbation of the band edges yielding a tailing of the absorption coefficient [31,59]. The tailing (also called characteristic) energy E_1 and the integrated absorption coefficient at a photon energy of 1.3 eV (see Fig. 6) rise up to a fluence of about 3×10^{14} cm^{-2}. This behavior can be explained by the formation of charged point defects in the whole implanted layer. Both quantities Kd and E_1 saturate at fluences above 3×10^{14} cm^{-2}. This suggests that the concentration of point defects remains constant at ion fluences above 3×10^{14} cm^{-2}. The characteristic energy reaches a saturation level of 0.57 eV, which is in good agreement with values of 0.50–0.52 eV determined in former works in case of a maximum concentration of point defects [7,9,10,44].

It is important to note that the optical subgap absorption of amorphous GaAs is connected with a much smaller characteristic energy of 0.16–0.18 eV [9,10]. This means, if amorphous regions are produced in a layer saturated with point defects, the presence of amorphous regions leads to a decrease of the characteristic energy. Such a decrease, although still small, is indicated for the ion fluence of 5×10^{15} cm^{-2}. Furthermore, for this fluence the transmission and reflection spectra exhibit more pronounced interference structures (see, e.g., [60] for similar effects in ion implanted SiC). This points to an increase of the refraction index of the implanted layer, which occurs in case of amorphous material only. Thus, the assumption of beginning amorphization of the implanted GaAs layer at ion fluences around 5×10^{15} cm^{-2} is not in contradiction with the measured optical properties.

IV. DISCUSSION

A. Defect types and evolution of strain

A summary of the fluence dependence of defect formation is presented in Fig. 6. Aside from the relative concentration of displaced lattice atoms $n_{\rm da}$ and the perpendicular strain $\epsilon_\perp$ (both taken at the depth of maximum), also the integrated absorption Kd and the integrated in-plane stress S are included. It should be mentioned that the latter two quantities do not refer to a certain depth but represent mean values over the entire implanted layer. The relative concentration of displaced lattice atoms $n_{\rm da}$ reaches a value of 0.14 (i.e., 14%) for an ion fluence of 2×10^{15} cm^{-2}. This fluence corresponds to a maximum Si concentration of 0.001 (i.e., 0.1 at.%). Therefore, it can be assumed that changes of the physical properties of the implanted layer are mainly related to the lattice defects rather than to any chemical effect of the implanted Si ions. Especially the optical subgap absorption clearly correlates with the energy deposited in nuclear collisions independent of the ion species applied [44]. This does not exclude the formation of point defects involving the implanted Si atoms, but their contribution to the total concentration of displaced lattice atoms cannot be separated. All physical quantities plotted in Fig. 6 increase in the same way up to an ion fluence of about 5×10^{13} cm^{-2}. This increase is attributed to the formation of individual point defects. Strain and optical absorption saturate and remain constant after a transition region up to about 3×10^{14} cm^{-2}. The in-plane stress increases only very weakly whereas the number of displaced lattice atoms clearly increases. This indicates the occurrence of a second type of defects for ion fluences above 1×10^{14} cm^{-2}, which manifests itself especially in the RBS/C data. Any hints for the existence of amorphous zones were only observed in case of the highest ion fluence applied of 5×10^{15} cm^{-2}. Hence, this second type of defects cannot be amorphous zones but must be some kind of defect clusters. From our results it can be concluded that these defect clusters affect strain and optical absorption of the implanted layer to a much lesser extent than point defects.

The analysis of the fluence dependence of quantities measuring radiation damage is a common method for obtaining more information about possible mechanism of damage formation (see Chap. 3 in [2]). Here, three types of defects were taken into account: point defects with fraction $n_{\rm pd}$, defect clusters with fraction $n_{\rm dc}$, and amorphous regions with fraction $n_{\rm a}$. The fluence dependence of $n_{\rm pd}$, $n_{\rm dc}$, and $n_{\rm a}$ is arranged as a system of coupled differential equations (see, e.g., [61–63])

$$\frac{dn_{\rm pd}}{dN_{\rm I}} = \sigma_{\rm pd}(1 - n_{\rm pd} - n_{\rm dc} - n_{\rm a}) - \sigma_{\rm r} n_{\rm pd} - (\sigma_{\rm dc} + \sigma_{\rm sc} n_{\rm dc} + \sigma_{\rm a} + \sigma_{\rm sa} n_{\rm a}) n_{\rm pd}, \quad (3)$$

$$\frac{dn_{\rm dc}}{dN_{\rm I}} = (\sigma_{\rm dc} + \sigma_{\rm sc} n_{\rm dc})\left(1 - \frac{n_{\rm pd} + n_{\rm dc}}{f_{\rm s}(1 - n_{\rm a})}\right) - (\sigma_{\rm a} + \sigma_{\rm sa} n_{\rm a}) n_{\rm dc}, \quad (4)$$

$$\frac{dn_{\rm a}}{dN_{\rm I}} = (\sigma_{\rm a} + \sigma_{\rm sa} n_{\rm a})(1 - n_{\rm a}), \quad (5)$$

which ensure that the total defect concentration $n_{\rm total} = n_{\rm pd} + n_{\rm dc} + n_{\rm a}$ does not exceed unity (i.e., 100%). The cross sections for defect production within a single ion impact are given by $\sigma_{\rm pd}$, $\sigma_{\rm dc}$, and $\sigma_{\rm a}$ for point defects, defect clusters, and amorphous regions, respectively. Amorphous zones can evolve in all areas, which are not yet amorphized. In the model it is assumed that point defects can be produced only within crystalline regions. Recombination of point defects is considered by means of the cross section $\sigma_{\rm r}$. Defect clusters and point defects are produced up to a saturation value of $f_{\rm s}$ in not yet amorphized regions. The cross sections $\sigma_{\rm sc}$ and $\sigma_{\rm sa}$ refer to a stimulated growth of defect clusters and amorphous regions, respectively, which may occur only if defects of the respective type already exist. It should be noticed that $\sigma_{\rm r}$, $\sigma_{\rm sc}$, and $\sigma_{\rm sa}$ are different from $\sigma_{\rm pd}$, $\sigma_{\rm dc}$, and $\sigma_{\rm a}$ with respect to their dimension.

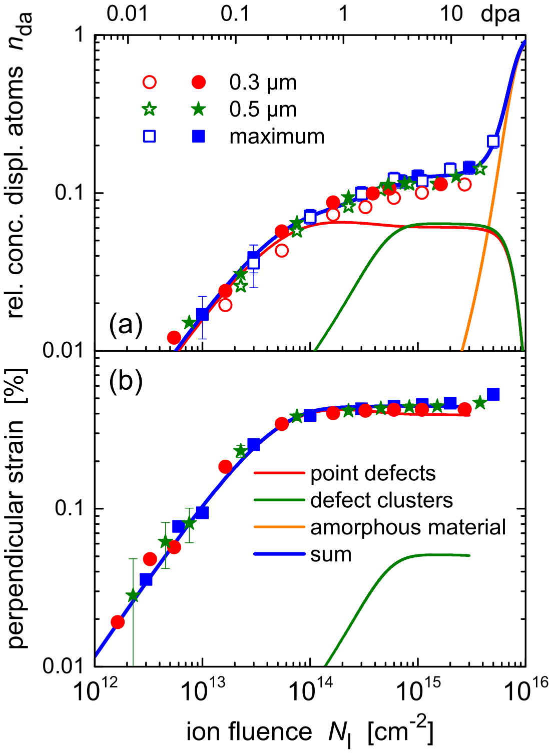

FIG. 7. Relative concentration of displaced lattice atoms n_{da} (a) and perpendicular strain $\epsilon_{\perp}$ (b) versus ion fluence N_{I}. Data taken at the maximum of the measured distributions are given as blue squares. The lines are fitted to these data using Eqs. (3)–(6). The corresponding parameters are given in Table I. In order to add data taken at 0.3 μm (circles) and 0.5 μm (stars), the ion fluences are converted into displacements per lattice atoms (dpa, upper scale). In (a) full symbols refer to analysis with 1.8 MeV and open symbols to 1.4 MeV He ions.

In order to extract the model parameters, model curves were fitted to the experimental data. Herein, the depth-integrated quantities were not taken into account. The total concentration n_{total} is assumed to be given by the relative number of displaced lattice atoms n_{da}, taken at the depth of maximum damage. The perpendicular strain at the depth of maximum damage is assumed to be related to the fraction of point defects and defect clusters according to

$$\epsilon_{\perp}(N_{\mathrm{I}}) = \alpha_{\mathrm{pd}} n_{\mathrm{pd}}(N_{\mathrm{I}}) + \alpha_{\mathrm{dc}} n_{\mathrm{dc}}(N_{\mathrm{I}}), \quad (6)$$

with α_{pd} and α_{dc} being fluence-independent parameters describing the strength of point defects (pd) and defect clusters (dc) in contributing to the maximum perpendicular strain. Experimental and calculated values of n_{da} and $\epsilon_{\perp}$ are presented in Fig. 7. Aside from the maximum values, data are included which were taken at depths of 0.3 and 0.5 μm. For this the ion fluences are converted into the number of displacements per atom dpa (see Sec. II). Within the experimental uncertainties, almost uniform dependencies of n_{da} and $\epsilon_{\perp}$ versus dpa are observed independent of the depth at which the data were taken. This demonstrates that the nuclear energy deposition of the implanted ions into displacement of lattice atoms (represented by the number of dpa) is the dominating cause of the observed radiation damage. It should be mentioned that there is a slight tendency of lower values occurring at the depth of 0.3 μm, which can be explained by some defect annealing due to the electronic energy loss of the implanted ions [64], which is highest close to the surface for 1 MeV Si ions irradiated in GaAs.

Model curves calculated with Eqs. (3)–(6) were fitted to n_{da} and $\epsilon_{\perp}$ measured in the maximum of the corresponding depth profiles by visual inspection. The optimum result is presented in Fig. 7 and the model parameters are given in Table I. According to the discussion above, a significant contribution of defect clusters and amorphous regions was restricted to ion fluences above 1×10^{14} and 3×10^{15} cm^{-2}, respectively, by choosing the direct impact cross sections σ_{dc} and σ_{a} as low as possible. It should be mentioned that the curves still can be fitted with values being larger by a factor of about 5. However, this does not change the general discussion of the processes given below. Figure 7 demonstrates that a very good fit of the experimental data is obtained applying the parameters given in Table I. This demonstrates that the processes behind Eqs. (3)–(5) are well capable for describing the physical mechanisms of damage formation in GaAs during 1 MeV Si ion implantation at room temperature. Assuming a circular shape, the diameter of the area damaged by one ion can be estimated from the cross sections σ_{dc} and σ_{a}. The corresponding values are below or of the order of the distance between two neighboring atoms. This is still true even if one assumes that these two cross sections could be larger by a factor of 5. This means a cluster produced within a direct ion impact would contain only one or two atoms. However, in this case neither an amorphous zone nor a defect cluster can be defined. Therefore, these cross sections do not represent an effect caused by direct ion impacts but act as substitute to emulate nucleation of defect clusters and amorphous nuclei, respectively. The fluence-independent parameters α_{pd} and α_{dc} [see Eq. (6) and Table I] were found to be 0.065 and 0.008, respectively. This shows that point defects contribute by a factor of about 8 more to the lattice strain than defect clusters.

The following scenario of damage formation can be deduced from our results. Only point defects remain after relaxation of the primary collision cascade at very low ion fluences, when each ion impinges on still pristine GaAs. The implantation temperature is the main reason for this behavior. Damage formation in ion implanted GaAs can be described within the concept of critical temperatures T_{c} (see [42,43] and Chap. 3 in [2]). Within this concept it is assumed that the

TABLE I. List of model parameters used for calculating the curves in Fig. 7 with Eqs. (3)–(6).

σ_{pd} (10^{-16} cm^2)	σ_{r} (10^{-15} cm^2)	σ_{dc} (10^{-16} cm^2)	σ_{sc} (10^{-16} cm^2)	f_{s}	σ_{a} (10^{-18} cm^2)	σ_{sa} (10^{-17} cm^2)	α_{pd}	α_{dc}
18	25	1	12	0.125	1	90	0.065	0.008

primarily produced damage clusters shrink due to thermally enhanced mobility and annihilation of intrinsic point defects. This explains the exponential increase of the ion fluence necessary for amorphization with increasing temperature T_I during implantation, which is observed in ion implanted GaAs and many other covalent-ionic materials (see Chap. 3 in [2]). At $T_I = T_c$ the amorphization fluence mathematically reaches infinity. This means no defects should remain from a single-ion impact. In case of GaAs an empirical formula was suggested to calculate the critical temperature (see [65] and references therein). For the implantation conditions applied here [number of displaced atoms per ion and unit depth N^*_{displ}=2.15/(ion Å) and ion flux 1.4 × 10^{11} s^{-1} cm^{-2}], a critical temperature of $T_c = 296$ K can be calculated, which corresponds to room temperature at which all experiments were done. Thus, our experiments were done right at the critical temperature for the applied implantation conditions. Indeed, the experimental results are in agrement with the predictions of the concept of critical temperatures because no heavily damaged or amorphous regions remain from single-ion impacts. Apparently, only point defects survive, the existence of which can be explained by not complete or imperfect recombination and annihilation of point defects. The effect of individual ion impacts sums up resulting in a linear increase of the defect concentration with increasing ion fluence at very low fluences. This is connected with an almost linear increase of the integral optical absorption and the lattice strain, which is clearly visible for ion fluences below 5×10^{13} cm^{-2} (see Figs. 6 and 7). The cross section of point-defect formation of $\sigma_{\text{pd}} = 1.8 \times 10^{-15}$ cm^2 [which follows from the increase of $n_{\text{da}}(N_I)$ at very low ion fluences] is much smaller than the cross section following from the SRIM calculations of $\sigma_{\text{SRIM}} = 4.9 \times 10^{-15}$ cm^2 (see Sec. II). This again proves the strong in-cascade annealing during relaxation of the primary collision cascades for the implantation conditions applied here.

When the ion fluence is further increased, ion impacts start to overlap and freshly produced point defects can recombine with those already existing from previous ion impacts. Hence, the balance between point-defect formation and recombination results in a saturation of the point-defect concentration. This is expressed in a saturation of the induced lattice strain and the optical absorption for ion fluences above 3×10^{14} cm^{-2} (see Figs. 6 and 7). The ability of defects to recombine or annihilate indicates that in this early stage of defect formation preferable individual point defects such as vacancies, interstitials, and antisite defects are produced. Obviously, the concentration of these point defects cannot exceed a critical value either because the strain in the material caused by defects cannot exceed a critical value or because of other reasons. It was already shown above that the defect clusters affect the strain within the implanted layer much weaker than point defects. This reveals a driving force for newly produced point defects to arrange in defect clusters. Consequently, a further increase of the ion fluence, i.e., a further introduction of point defects results in the formation of small defect clusters. Their microstructure seems to ensure that no further strain increase within the implanted layer takes place [see Fig. 7(b)]. To some extent, this behavior is similar to the behavior of foreign atoms in a solid. When the thermal solid-solubility limit is exceeded, a further introduction of foreign atoms results in precipitation of these atoms. The relative concentration of point defects and defect clusters saturates at 0.125 which is in agreement with previous results for N ion implanted GaAs [65].

The nature of the defect clusters is difficult to identify. Energy-dependent RBS/C studies revealed a contribution of correlated displaced lattice atoms. This could be small extended defects or slightly misaligned crystalline regions. Extended defects could not be detected in our TEM study (see Fig. 3). In previous high-resolution TEM investigations on GaAs implanted with 1 MeV Si ions to an ion fluence of 3×10^{15} cm^{-2}, defect structures were detected and denoted as interstitial dislocations lying in the {111} planes [66]. This is different to our findings. Dislocation loops were also detected in GaAs implanted with Zn ions at a slightly elevated temperature of 110 °C [67]. It was already mentioned above that damage formation in GaAs at temperatures around RT is very sensitive to the beam current during implantation. In Ref. [66] a beam current of about 0.5 μA cm^{-2} was applied. The beam current used in our experiments was more than one order of magnitude lower (0.025 μA cm^{-2}, see Sec. II). Therefore, it can be assumed that the temperature within the implanted layer during the implantation was higher for the previous experiments [66]. A higher temperature increases the mobility of defects and thus yields better conditions for the growth of dislocation loops. Furthermore, it has to be noticed that our TEM studies were performed for a slightly lower ion fluence. From these considerations it can be assumed that for our sample investigated by TEM dislocation loops had not yet been formed, or could not be found because they had formed with a very low concentration.

The occurrence of small dark areas with a size of few nanometers in the TEM images has been observed in other ion-irradiated materials, too, as for instance in UO_2 [68,69], in SiC [70], and in various metals [71,72]. They are called "black dot defects." They manifest irradiation-induced defect clusters, but no clear conclusion as to the nature or microstructure of these defect clusters can be given. Only after further increasing the ion fluence during irradiation, extended defects such as dislocation loops can be well identified in the TEM images.

Recently, Gala and Zollo investigated complexes of interstitials I_n with $n \leqslant 7$ in GaAs as possible core-basic structures for nucleation and growth of extended defects [73]. In the frame of the adopted approach and the limits of the used semiempirical parametrization, As_3Ga_2 (I_5) was identified as the most stable complex against the neighbors (I_4 and I_6). Based on these studies and the discussion above, it is possible to assume that the dark areas of local strain visible in the TEM images (see Fig. 3) are caused by As_3Ga_2 clusters.

From Fig. 7(a) it can be seen that a third stage of damage formation is to be expected at ion fluences above 3×10^{15} cm^{-2}. This stage is ion-beam-induced amorphization of the implanted layer. It is known to occur in GaAs at $T_I \approx T_c$ but only by secondary processes such as nucleation and growth of amorphous nuclei [65]. In this case, nucleation of amorphous seeds may proceed at the interface between highly defective and crystalline regions [42]. A buried defect band may inhibit the diffusion of defects and thus promote the nucleation of amorphous seeds [74]. However, the process of amorphization is not within the scope of this paper.

It was already mentioned above that defect formation in GaAs implanted with 1 MeV Si ions is similar as for implantation with 280/325 keV N or 2 MeV Se ions at RT. Room temperature corresponds to the critical temperature for 280/325 keV N ions [65]. For the Se ion implantation a beam current of 3.5 nA/cm^2 (ion flux of 2.2×10^{10} cm^{-2} s^{-1}) was given [36]. With $N^*_{\text{displ}} = 7.8/(\text{ion Å})$ in the maximum of the distribution (calculated as explained in Sec. II) the critical temperature for 2 MeV Se ion implantation in GaAs is estimated to 301 K. Consequently, all three cases have in common that implantation is performed at about the critical temperature for the respective implantation conditions. Therefore, it can be concluded that the results given here for 1 MeV Si ions are representative for ion implantation in GaAs at or near the respective critical temperature.

B. Evolution of in-plane stress

In previous papers, the evolution of in-plane stress in ion implanted materials as a function of the ion fluence was described taking into account the following three processes [27,28]. (i) Ion-beam-induced damage strains the surrounding crystal matrix in crystalline materials. This leads to changes of the density within the implanted layer and thus to the formation of in-plane stress. (ii) Stress relaxation takes place by radiation-induced plastic flow. (iii) Finally, stress saturation is observed at high-ion fluences which is commonly explained by anisotropic deformation. For the implantation conditions applied in the respective works, amorphization was the dominating process. Particularly processes (ii) and (iii) were attributed to the known behavior of amorphous material (see also [75]). The situation is completely different in our case of Si ion implanted GaAs. No indications of amorphization were observed in the ion fluence range of the curvature measurement (i.e., up to 1.1×10^{15} cm^{-2}). Therefore, only damage-induced in-plane stress formation is taken into account here. It is assumed that point defects and defect clusters contribute to the total integrated in-plane stress S according to

$$S(N_{\text{I}}) = S^*_{\text{pd}} n^{\text{int}}_{\text{pd}}(N_{\text{I}}) + S^*_{\text{dc}} n^{\text{int}}_{\text{dc}}(N_{\text{I}}). \tag{7}$$

Herein, $n^{\text{int}}_{\text{pd}}$ and $n^{\text{int}}_{\text{dc}}$ are the depth-integrated concentrations of point defects and defect clusters, respectively. Their fluence dependencies were obtained by fitting the relative concentration of displaced lattice atoms integrated over depth $n^{\text{int}}_{\text{da}} = \int_0^{t_{\text{imp}}} n_{\text{da}}(z)dz$ and the integrated perpendicular strain $\epsilon^{\text{int}}_{\perp} = \int_0^{t_{\text{imp}}} \epsilon_{\perp}(z)dz$ using Eqs. (3)–(5) (without contribution of amorphous material) and Eq. (6), respectively (not shown). Now, $S(N_{\text{I}})$ according to Eq. (7) can be fitted to the measured values by adjusting the effectivities S^*_{pd} and S^*_{dc} of point defects and defect clusters, respectively, contributing to the in-plane stress S. From Fig. 8 it can be seen that a good representation of the experimental data is achieved for ion fluences above 1×10^{14} cm^{-2} yielding the fluence-independent parameters $S^*_{\text{pd}} = 0.405$ N/m^2 and $S^*_{\text{dc}} = 0.065$ N/m^2. Thus, point defects (with concentrations around saturation) contribute by a factor of about 6 more to the total stress than defect clusters. This is in good agreement with the findings for the perpendicular strain, for which a factor of 8 was obtained (see Table I). For ion fluences below 1×10^{14} cm^{-2}, the calculated in-plane stress S is lower than the measured one. As this fluence range is dominated by point defects, two point-defect-related scenarios are possible for explaining this deviation. First, different types of point defects may exist. They may exhibit a different fluence dependence and contribute with different effectivities to the total in-plane stress. Second, the effectivity S^*_{pd} is no more constant but varies as a function of ion fluence, i.e., as a function of the point-defect concentration. The first scenario was successfully applied to explain the in-plane stress evolution in ion implanted LiNbO$_3$ measured in different crystallographic directions [29]. Specifically, in one direction a bimodal fluence dependence of S was found, which clearly indicated the transformation of one defect type into another accompanied by a change in effectivity. In our case, such indications do not exist. Therefore, the second scenario is assumed to occur. S^*_{pd} was modified to fit the experimental data also at low ion fluences (see Fig. 8). The thus obtained dependence $S^*_{\text{pd}}(N_{\text{I}})$ is plotted in Fig. 9. It can be clearly seen that the effectivity of point defects in contributing to in-plane stress decreases with increasing ion fluence. A change of defect parameters, more specifically of defect migration parameters, with radiation fluence was also found for other crystalline materials irradiated with energetic particles in a regime with no amorphization occurring [76]. The obvious decrease of S^*_{pd} with increasing ion fluence corresponds to a continuous decrease with increasing point-defect concentration (cf. Figs. 7 and 8). Such a behavior can be explained by a partial compensation of the strain fields of individual point defects with decreasing distance between each other. Another interpretation is to assume that already at these low defect concentrations an ion-beam-induced relaxation takes place. Such an effect was already found for H ion implanted silicon [77]. It was concluded from the decrease of the shear modulus of the implanted layer (effective value over the entire implanted layer) μ_{imp}, below the value of the unimplanted

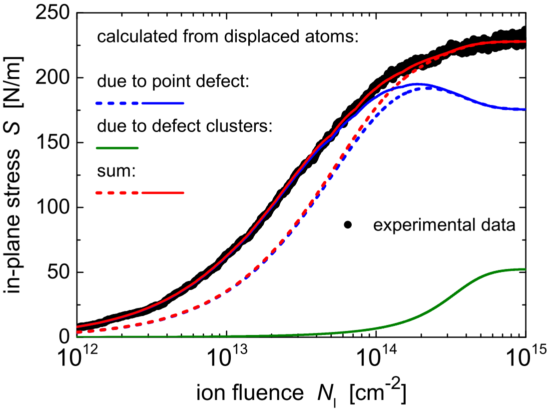

FIG. 8. Integrated in-plane stress S versus ion fluence N_{I} measured *in situ* (black dots). The stress calculated with Eq. (7) is given as red line with the contributions of point defects (blue lines) and defect clusters (green line). Dashed lines refer to a constant efficiency of point defects contributing to S, whereas for the solid lines a fluence-dependent efficiency of point defects (see Fig. 9) was used.

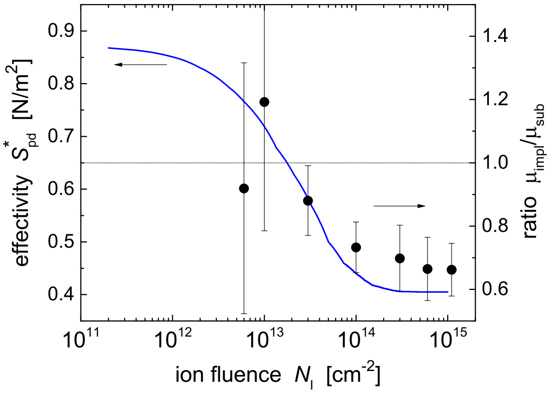

FIG. 9. Efficiency S^*_{pd} of point defects contributing to the total in-plane stress S (blue line, left scale) and ratio $\mu_{\mathrm{impl}}/\mu_{\mathrm{sub}}$ of shear modulus of implanted layer and substrate (symbols, right scale) versus ion fluence N_{I}.

substrate μ_{sub}. The ratio $\mu_{\mathrm{imp}}/\mu_{\mathrm{sub}}$ was estimated from XRD and curvature data according to [77]

$$\frac{\mu_{\mathrm{imp}}}{\mu_{\mathrm{sub}}} = -\frac{(1+\nu_{\mathrm{sub}})\, t_{\mathrm{sub}}^2}{6\,(1-\nu_{\mathrm{sub}})\, R\, \epsilon_\perp^{\mathrm{int}}}. \tag{8}$$

Herein, the measured fluence dependencies of the radius R of curvature (see Sec. II) and the integrated perpendicular strain $\epsilon_\perp^{\mathrm{int}}$ were used. ν_{sub} is Poisson's ratio of the GaAs substrate with $\nu_{\mathrm{sub}} = 0.31$ [58]. $\mu_{\mathrm{imp}}/\mu_{\mathrm{sub}}$ is shown versus fluence in Fig. 9. Up to 3×10^{13} cm^{-2} a ratio of one lies in the range of the error bars. This indicates that the elastic properties of the implanted layer did not change in comparison to those of the substrate. But, for higher fluences the effective shear modulus of the implanted layer decreases below the value of the substrate. The ratio $\mu_{\mathrm{imp}}/\mu_{\mathrm{sub}}$ reaches a value of ≈ 0.65 for 1.1×10^{15} cm^{-2}. This value is comparable to that found for H ion implanted Si of about 0.5 [77]. Thus, our studies confirm that in ion-implanted semiconductors dramatic effects on the shear modulus occur at rather low damage levels far away from complete amorphization. The implanted layers accommodate to the increasing defect concentration by a fluence-dependent softening of the elastic constants. Within our approach, this effect exhibits in the decrease of the effectivity of point defects in contributing to the total in-plane stress with increasing ion fluence (see Fig. 9). A similarly strong softening of the shear modulus by a factor of 0.5 was found in zircon but when amorphized by radiation damage [78]. Even though zircon is a completely different material than GaAs, the result shows that such strong changes of the shear modulus are usually to expect after amorphization. It seems to be obvious that the mechanisms are different that cause the decrease of the shear modulus in amorphized zircon (see also [79]) and in weakly damaged semiconductors. For understanding the latter, more investigations are necessary.

C. Estimation of point-defect concentration

As discussed above, during the early stage of damage formation at low ion fluences (below 5×10^{13} cm^{-2}) individual point defects such as vacancies and interstitials (Frenkel pairs) and antisite defects are expected to be produced. For estimating the concentration of point defects, a procedure is applied that was used recently for ion-irradiated MgO [80] and SiC [81]. In the presence of point defects, the change of the unconstrained lattice parameter $(\Delta a/a)_{\mathrm{r}}$, which is also called relaxed lattice parameter or defect-induced strain [48], can be connected with the defect concentration by [83–85]

$$\left(\frac{\Delta a}{a}\right)_{\mathrm{r}} = \frac{1}{3}\sum_i n_{\mathrm{i}} \frac{\Delta v_{\mathrm{i}}}{\Omega}, \tag{9}$$

where n_{i} denotes the relative defect concentration of the ith sort of defects with a relaxation volume of Δv_{i} expressed in units of the average atomic volume Ω. The volume change of an interstitial is positive, in contrast to a vacancy, which typically induces a negative change [45]. Pillukat *et al.* [86] investigated GaAs after low-temperature 3 MeV electron irradiation and subsequent thermal annealing. They identified Frenkel pairs annealing around RT (stage I,II) and at about 500 K (stage III) in agreement with previous work by Thommen [87] who introduced the annealing stages. By evaluating Huang diffuse x-ray scattering, Pillukat *et al.* determined the relaxation volume of the corresponding Frenkel pairs. In case of the stage (I,II) Frenkel pairs, relaxation volumes of $\Delta v_{\mathrm{I}}^{\mathrm{I,II}} = (1.9 \pm 0.3)\Omega$ for interstitials and $\Delta v_{\mathrm{V}}^{\mathrm{I,II}} = -(0.55 \pm 0.10)\Omega$ for vacancies were found. In case of stage (III) Frenkel pairs values of $\Delta v_{\mathrm{I}}^{\mathrm{III}} = 0.8^{+0.1}_{-0.3}\Omega$ for interstitials and $\Delta v_{\mathrm{V}}^{\mathrm{III}} = -(0.08 \pm 0.08)\Omega$ for vacancies were estimated. It was proposed that the stage (I,II) Frenkel pairs may represent gallium vacancies and the stage (III) Frenkel pairs may constitute defects on the arsenic sublattice [86].

Although the RBS analysis suggests interstitial atoms to be an important component of the point defects (see Sec. III A), their microstructure cannot be ascertained from our data. However, in order to get an estimate of the point-defect concentration, it is assumed that Frenkel pairs are the main type of point defects in the Si ion implanted GaAs layers. The approximate relaxation volumes of Frenkel pairs in GaAs are deduced from the results of Pilukat *et al.* given above. This shall not imply that damage formation in GaAs is equivalent for 1 MeV Si ions and 3 MeV electrons. It just means that Frenkel pairs are taken to approximate the defects existing after 1 MeV Si ion implantation. This corresponds to the approach used for ion-implanted MgO [80] and SiC [81].

For the following estimations, relaxation volumes of $\Delta v_{\mathrm{I,II}} = (1.4 \pm 0.4)\Omega$ and $\Delta v_{\mathrm{III}} = 0.7^{+0.2}_{-0.4}\Omega$ were applied. Under the assumption of tetragonal distortion (which has been verified here as the parallel strain is more than one order of magnitude smaller than the maximum perpendicular strain), the relative change of the relaxed lattice parameter $(\Delta a/a)_{\mathrm{r}}$ can be related to the measured perpendicular strain [85,88,89]. With Eq. (9) one finally obtains

$$\left(\frac{\Delta a}{a}\right)_\perp = \frac{1+\nu_{\mathrm{imp}}}{1-\nu_{\mathrm{imp}}}\left(\frac{\Delta a}{a}\right)_{\mathrm{r}} = \frac{1}{3}\,\frac{1+\nu_{\mathrm{imp}}}{1-\nu_{\mathrm{imp}}}\,\frac{\Delta v}{\Omega}\, n_{\mathrm{FP}}. \tag{10}$$

Herein, $(\Delta a/a)_\perp = \epsilon_\perp$ is the strain perpendicular to the surface [see Eq. (1)] and ν_{imp} is the Poisson ratio of the implanted layer. It follows that the concentration of Frenkel pairs n_{FP} is directly proportional to the perpendicular strain $\epsilon_\perp$. In correspondence to the fluence dependence of the maximum perpendicular strain (see Fig. 7), the concentration of Frenkel pairs increases up to about 1×10^{14} cm^{-2} and the saturation level follows to ≈0.5% for the stage (I,II) Frenkel pairs and ≈0.9% for the stage (III) Frenkel pairs (assuming $\nu_{\rm imp} = \nu_{\rm sub}$). It should be noticed that this is not necessarily the number of defect centers within the implanted layer. According to the principles of the superposition model [80,82], the displacement fields of point defects simply superimpose when forming complexes. This means the assumed Frenkel pairs can be regarded as building blocks for larger point-defect complexes, which may exist in the ion implanted layers. The Frenkel pairs also act to approximate the effect of antisite defects that can expand the lattice as well [46]. The superposition model and correspondingly Eq. (9) are valid as long as the complexes remain small (i.e., below the size of a dislocation loop) and the defects to not interact, which is fulfilled in our case.

The contribution of point defects to the total strain is given by $\alpha_{\rm pd} n_{\rm pd}$ (see Eq. (6)). Then, the number of displaced lattice atoms per Frenkel pair $n_{\rm pd}/n_{\rm FP}$ follows to

$$\frac{n_{\rm pd}}{n_{\rm FP}} = \frac{1+\nu_{\rm imp}}{3(1-\nu_{\rm imp})}\frac{\Delta v}{\Omega}\frac{1}{\alpha_{\rm pd}}. \tag{11}$$

In case of stage (I,II) Frenkel pairs the number of displaced atoms per Frenkel pair is estimated to 14 ± 4 and for stage (III) Frenkel pairs to 7 ± 3. The number of displaced atoms in case of different kinds of point defects was investigated for silicon using computer simulations [35,90]. In [90] only atoms with displacement distances larger than 0.11 Å (the 2D root-mean-square vibrational amplitude) were considered since only these atoms interact with the channeled ion beam. A number of displaced atoms of 6, 4, 9, 4, and 4 is found for the elementary hexagonal interstitial, the tetrahedral interstitial, the split interstitial, the bond defect, and the vacancy, respectively. In [35] a different potential was used for the calculations and the minimum displacement distance was restricted to values larger than 0.2 Å. In this case, 10 atoms per ⟨110⟩ split interstitial and 18 atoms per divacancy [35] were obtained. In this study, GaAs and not silicon is investigated. Nevertheless, the here estimated numbers of displaced atoms per Frenkel pair is of the same order of magnitude as those obtained from simulations for point defects in silicon. As already mentioned above, the interstitial complex $\rm As_3Ga_2$ (I_5) was identified as possible nucleation seed for extended defect complexes in GaAs. The atomic configuration of that complex was evaluated to determine the number of displaced atoms with displacement distances larger than 0.1 Å (the 2D root mean square of Ga and As) projected to the ⟨100⟩ direction. A value of 42 was found, which corresponds to ≈8 displaced atoms per interstitial. This value is in fair agreement with the values of 14 ± 4 and 7 ± 3 displaced atoms per Frenkel pair estimated above from the experimental data presented here.

The fluence dependence in Fig. 7 shows that point defects occur over a wide range of ion fluences. As already mentioned above, it can not be assumed that they consist of Frenkel pairs only. Especially when saturation of point defects begins, it is to be expected that the microstructure changes and larger point-defect complexes form. However, our estimations demonstrate that both simple and more complex point-defect structures result in similar numbers of displaced lattice atoms per interstitial atom involved as the main base of lattice distortion. Obviously, our results support the superposition principle mentioned above.

V. SUMMARY AND CONCLUSION

Damage formation in ⟨100⟩ oriented GaAs implanted with 1 MeV Si ions to ion fluences between 3×10^{12} and 5×10^{15} cm^{-2} at room temperature was scrutinized by applying different experimental techniques. Rutherford backscattering spectrometry in channeling configuration (RBS/C) with He ions, performed at two different target temperatures, provided the mean displacement distance of atoms from their original lattice sites as well as the concentration of displaced lattice atoms versus depth. RBS/C with He ions of different beam energies indicated the existence of defects being connected with correlated displaced lattice atoms at higher ion fluences. These could be extended defects of slightly misaligned crystalline regions. X-ray diffraction (XRD) allowed to determine the depth distribution of perpendicular strain in the implanted layers. Subgap optical spectroscopy yielded the integrated absorption coefficient. The buildup of integrated in-plane stress as a function of the ion fluence was obtained from a curvature measurement done *in situ* during the implantation. A GaAs layer implanted with a selected ion fluence was studied by high-resolution transmission electron microscopy (TEM).

A common damage evolution model was used to represent the fluence dependence of the measured quantities up to about 2×10^{15} cm^{-2}. Herein, point defects and defect clusters had to be taken into account. The beginning of amorphization is indicated for higher ion fluences, but this process is not within the scope of this work. It is shown that point defects contribute by a factor of 8 more to the lattice strain than defect clusters. When the concentration of point defects or the induced lattice strain reach a saturation value, which obviously cannot be exceeded, newly produced point defects arrange in defect clusters. This mechanism ensures that no further increase of the lattice strain occurs and thus reveals a driving force for the formation of defect clusters. The microscopic structure of the defect clusters cannot be resolved from our data. $\rm As_3Ga_2$ interstitial complexes are suggested as possible structure. Regarding the in-plane stress, point defects contribute again at least by a factor of 6 more than defect clusters. The efficiency of point defects in contributing to the total in-plane stress decreases with increasing point-defect concentration. This can be related to a significant decrease of the shear modulus of the implanted layer below the value of pristine GaAs. Such an effect is commonly expected and observed when amorphizing a material. We measured the reduced shear modulus for a very low level of damage in GaAs in agreement with similar studies on proton-irradiated silicon. Such processes occurring already at low defect concentrations may have significant implications when implanting nanostructured materials.

From our results, the number of displaced lattice atoms per interstitial atom as the main cause for lattice distortion is estimated to be about 10. This is in fair agreement with corresponding numbers for individual point defects in silicon, varying between 4 and 18 depending on the point-defect type. In case of the $\rm As_3Ga_2$ interstitial complex, 8 displaced lattice atoms per interstitial atom were found, which is again in good agreement with our experimentally determined value. This means the number of displaced lattice atoms per interstitial atom is about the same independent of the microstructure of the defects. This result supports the superposition principle that the displacement fields of point defects superimpose when forming complexes.

In summary, the application of various techniques of analysis and combining measured quantities on a quantitative level reveals a deeper understanding of the mechanisms of defect formation as well as on the possible structure of defects in GaAs implanted with 1 MeV Si ions at room temperature. The chosen implantation parameters result in conditions for which only point defects remain after relaxation of the primary collision cascades (implantation at or near the critical temperature). Therefore the results can be taken as representative for GaAs implanted with other ion species and ion energies for which this condition is fulfilled.

ACKNOWLEDGMENTS

The authors would like to thank Dr. W. Wesch, Dr. K. Gärtner, Dr. S. Höfer, and Dr. M. Ghorbani-Asl for helpful discussions. We wish to thank U. Barth for carrying out the implantations and for his assistance during the RBS/C measurements. We thank C. Voigt for the preparation of the TEM lamella and H. Marschner for characterizing the GaAs samples by x-ray topography.

[1] M. Nastasi and J. Mayer, *Ion Implantation and Synthesis of Materials* (Springer, Berlin, 2006).
[2] *Ion Beam Modification of Solids*, edited by W. Wesch and E. Wendler (Springer, Berlin, 2016).
[3] A. Meldrum, R. Lopez, R. H. Magruder, L. A. Boatner, and C. W. White, in *Material Science with Ion Beams*, edited by H. Bernas (Springer, Berlin, 2010), p. 255.
[4] U. Zammit, K. N. Madhusoodanan, F. Scudieri, F. Mercuri, E. Wendler, and W. Wesch, Phys. Rev. B **49**, 2163 (1994).
[5] E. Wendler, P. Müller, T. Bachmann, and W. Wesch, J. Non-Cryst. Solids **176**, 85 (1994).
[6] E. Wendler, A. Heft, W. Wesch, G. Peiter, and H. H. Dunken, Nucl. Instrum. Methods Phys. Res., Sect. B **127-128**, 341 (1997).
[7] E. Wendler, W. Wesch, and G. Götz, Phys. Status Solidi A **112**, 289 (1989).
[8] E. Wendler and W. Wesch, Nucl. Instrum. Methods Phys. Res., Sect. B **73**, 489 (1993).
[9] U. Zammit, M. Marinelli, R. Pizzoferrato, and F. Mercuri, Phys. Rev. B **46**, 7515 (1992).
[10] W. Wesch, E. Wendler, and G. Götz, Nucl. Instrum. Methods Phys. Res., Sect. B **22**, 532 (1987).
[11] F. Urbach, Phys. Rev. **92**, 1324 (1953).
[12] W. Wesch, E. Wendler, G. Götz, K. Unger, H. Röppischer, and Chr. Resagk, Phys. Status Solidi B **130**, 539 (1985).
[13] G. Rey, G. Larramona, S. Bourdais, C. Chone, B. Delatouche, A. Jacob, G. Dennler, and S. Siebentritt, Sol. Energy Mater. Sol. Cells **179**, 142 (2018).
[14] A. Jordanov, Ph.D. thesis, University of Jena, 1988.
[15] K. Gärtner, K. Hehl, and G. Schlotzhauer, Nucl. Instrum. Methods Phys. Res. **216**, 275 (1983).
[16] K. Gärtner, K. Hehl, and G. Schlotzhauer, Nucl. Instrum. Methods Phys. Res., Sect. B **4**, 55 (1984).
[17] K. Gärtner, Nucl. Instrum. Methods Phys. Res., Sect. B **132**, 147 (1997).
[18] K. Gärtner, Nucl. Instrum. Methods Phys. Res., Sect. B **227**, 522 (2005).
[19] B. Breeger, E. Wendler, W. Trippensee, C. Schubert, and W. Wesch, Nucl. Instrum. Methods Phys. Res., Sect. B **174**, 199 (2001).
[20] B. Breeger, Ph.D. thesis, University of Jena, 2000.
[21] *High Energy Ion Beam Analysis of Solids*, edited by G. Götz and K. Gärtner (Akademie-Verlag, Berlin, 1988).
[22] M. Souilah, A. Boulle, and A. Debelle, J. Appl. Crystallogr. **49**, 311 (2016).
[23] S. Takagi, Acta Crystallogr. **15**, 1311 (1962).
[24] D. Taupin, Bull. Soc. Fr. Minéral. Cristallogr. **87**, 469 (1964).
[25] S. Takagi, J. Phys. Soc. Jpn. **26**, 1239 (1969).
[26] P. Flinn, D. Gardner, and W. Nix, IEEE Trans. Electron Devices **34**, 689 (1987).
[27] C. A. Volkert, J. Appl. Phys. **70**, 3521 (1991).
[28] T. Steinbach, A. Reupert, E. Schmidt, and W. Wesch, Nucl. Instrum. Methods Phys. Res., Sect. B **307**, 194 (2013).
[29] E. Schmidt, T. Steinbach, and W. Wesch, J. Phys. D: Appl. Phys. **47**, 265302 (2014).
[30] E. P. EerNisse, Appl. Phys. Lett. **18**, 581 (1971).
[31] V. L. Bonch-Bruevich, Phys. Status Solidi B **42**, 35 (1970).
[32] J. P. Biersack and J. F. Ziegler, *The Stopping and Ranges of Ions in Matter*, Vol. 1 (Pergamon, Oxford, 1985); see also www.srim.org.
[33] R. Bäuerlein, Z. Phys. **176**, 498 (1963).
[34] W. Wesch, A. Jordanov, K. Gärtner, and G. Götz, Nucl. Instrum. Methods Phys. Res., Sect. B **39**, 445 (1989).
[35] B. Weber, E. Wendler, K. Gärtner, D. M. Stock, and W. Wesch, Nucl. Instrum. Methods Phys. Res., Sect. B **118**, 113 (1996).
[36] E. Wendler, F. Schrempel, P. Müller, K. Gärtner, and W. Wesch, Nucl. Instrum. Methods Phys. Res., Sect. B **118**, 367 (1996).
[37] W. Wesch, K. Gärtner, A. Jordanov, and G. Götz, Nucl. Instrum. Methods Phys. Res., Sect. B **45**, 446 (1990).
[38] W. Wesch and E. Wendler, Nucl. Instrum. Methods Phys. Res., Sect. B **80-81**, 716 (1993).
[39] E. Wendler, W. Wesch, and G. Götz, Nucl. Instrum. Methods Phys. Res., Sect. B **52**, 57 (1990).
[40] W. Wesch, E. Wendler, and N. Dharmarasu, Nucl. Instrum. Methods Phys. Res., Sect. B **175-177**, 257 (2001).
[41] T. E. Hayes and O. W. Holland, Appl. Phys. Lett. **59**, 452 (1991).
[42] R. A. Brown and J. S. Williams, J. Appl. Phys. **81**, 7681 (1997).
[43] R. A. Brown and J. S. Williams, Phys. Rev. B **64**, 155202 (2001).
[44] E. Wendler, W. Wesch, and G. Götz, Phys. Status Solidi A **93**, 207 (1986).
[45] S. Qadri, M. Yousuf, C. Kendziora, B. Nachumi, R. Fischer, J. Grun, M. Rao, J. Tucker, S. Siddiqui, and M. Ridgway, Appl. Phys. A **79**, 1971 (2004).

[46] T. E. M. Staab, R. M. Nieminen, J. Gebauer, R. Krause-Rehberg, M. Luysberg, M. Haugk, and Th. Frauenheim, Phys. Rev. Lett. **87**, 045504 (2001).

[47] N. Sousbie, L. Capello, J. Eymery, F. Rieutord, and C. Lagahe, J. Appl. Phys. **99**, 103509 (2006).

[48] A. Debelle and A. Declemy, Nucl. Instrum. Methods Phys. Res., Sect. B **268**, 1460 (2010).

[49] P. Zaumseil, U. Winter, F. Cembali, M. Servidori, and Z. Sourer, Phys. Status Solidi A **100**, 95 (1987).

[50] V. S. Speriosu, B. M. Paine, M.-A. Nicolet, and H. L. Glass, App. Phys. Lett. **40**, 604 (1982).

[51] B. M. Paine and V. S. Speriosu, J. Appl. Phys. **62**, 1704 (1987).

[52] G. Kuri, G. Materlik, V. Hagen, and R. Wiesendanger, J. Vac. Sci. Technol. B **21**, 1134 (2003).

[53] B. M. Paine, N. N. Hurvitz, and V. S. Speriosu, J. Appl. Phys. **61**, 1335 (1987).

[54] G. P. Nair, K. Chandrasekaran, A. Narsale, B. Arora, and M. Gokhale, Nucl. Instrum. Methods Phys. Res., Sect. B **184**, 515 (2001).

[55] C. R. Wie, T. Vreeland, and T. A. Tombrello, MRS Proc. **35**, 305 (1984).

[56] V. S. Speriosu and T. Vreeland, J. Appl. Phys. **56**, 1591 (1984).

[57] G. C. A. M. Janssen, M. M. Abdalla, F. van Keulen, B. R. Pujada, and B. van Venrooy, Thin Solid Films **517**, 1858 (2009).

[58] Database: http://www.ioffe.ru/SVA/NSM/Semicond/.

[59] J. I. Pankove, Phys. Rev. **140**, A2059 (1965).

[60] E. Wendler and G. Peiter, J. Appl. Phys. **87**, 7679 (2000).

[61] N. Hecking, K. Heidemann, and E. T. Kaat, Nucl. Instrum. Methods Phys. Res., Sect. B **15**, 760 (1986).

[62] C. S. Schnohr, E. Wendler, K. Gärtner, W. Wesch, and K. Ellmer, J. Appl. Phys. **99**, 123511 (2006).

[63] E. Wendler, E. Treiber, J. Baldauf, S. Wolf, and C. Ronning, Nucl. Instrum. Methods Phys. Res., Sect. B **379**, 85 (2016).

[64] W. Wesch, E. Wendler, T. Bachmann, and O. Herre, Nucl. Instrum. Methods Phys. Res., Sect. B **96**, 290 (1995).

[65] E. Wendler, B. Breeger, C. Schubert, and W. Wesch, Nucl. Instrum. Methods Phys. Res., Sect. B **147**, 155 (1999).

[66] G. Braunstein, D. Tuschel, S. Chen, and S.-T. Lee, J. Appl. Phys. **66**, 3515 (1989).

[67] G. Zollo, C. Pizzuto, G. Vitali, M. Kalitzova, and D. Manno, J. Appl. Phys. **88**, 1806 (2000).

[68] Y. Haddad, L. Delauche, A. Gentils, and F. Garrido, Nucl. Instrum. Methods Phys. Res., Sect. B **435**, 25 (2018).

[69] L.-F. He, M. Gupta, C. A. Yablinsky, J. Gan, M. A. Kirk, X.-M. Bai, J. Pakarinen, and T. R. Allen, J. Nucl. Mater. **443**, 71 (2013).

[70] Y. R. Lin, L. G. Chen, C. Y. Hsieh, M. T. Chang, K. Y. Fung, A. Hu, S. C. Lo, F. R. Chen, and J. J. Kai1, Sci. Rep. **7**, 14635 (2017).

[71] C. Lu, K. Jin, L. K. Béland, F. Zhang, T. Yang, L. Qiao, Y. Zhang, H. Bei, H. M. Christen, R. E. Stoller, and L. Wang, Sci. Rep. **6**, 19994 (2016).

[72] O. Srba, J. Michalicka, E. Keilova, and J. Kocik, IEEE Trans. Nucl. Sci. **61**, 2149 (2014).

[73] F. Gala and G. Zollo, Phys. Rev. B **80**, 174113 (2009).

[74] E. Wendler, Nucl. Instrum. Methods Phys. Res., Sect. B **267**, 2680 (2009).

[75] E. Snoeks, A. Polman, and C. A. Volkert, Appl. Phys. Lett. **65**, 2487 (1994).

[76] E. Kotomin, V. Kuzovkov, A. I. Popov, J. Maier, and R. Vila, J. Phys. Chem. A **122**, 28 (2018).

[77] S. Reboh, F. Rieutord, L. Vignoud, F. Mazen, N. Cherkashin, M. Zussy, D. Landru, and C. Deguet, Appl. Phys. Lett. **103**, 181911 (2013).

[78] E. K. H. Salje, Appl. Phys. Lett. **89**, 131902 (2006).

[79] T. Beirau, W. D. Nix, R. C. Ewing, H. Pöllmann, and E. K. H. Salje, Appl. Phys. Lett. **112**, 201901 (2018).

[80] D. Bachiller-Perea, A. Debelle, L. Thome, and J.-P. Crocombette, J. Mater. Sci. **51**, 1456 (2015).

[81] A. Boulle, A. Debelle, J. B. Wallace, L. B. Bayu Aji, and S. O. Kucheyev, Acta Mater. **140**, 250 (2017).

[82] P. H. Dederichs, J. Phys. F: Met. Phys. **3**, 471 (1973).

[83] P. Ehrhart, J. Nucl. Mater. **216**, 170 (1994).

[84] M. W. Thompson, *Defects And Radiation Damage In Metals* (Cambridge University Press, Cambridge, 1969).

[85] A. Gaber, H. Zillgen, P. Ehrhart, P. Partyka, and R. S. Averback, J. Appl. Phys. **82**, 5348 (1997).

[86] A. Pillukat, K. Karsten, and P. Ehrhart, Phys. Rev. B **53**, 7823 (1996).

[87] K. Thommen, Rad. Effects **2**, 201 (1979).

[88] S. N. G. Chu, A. T. Macrander, K. E. Strege, and W. D. Johnston, J. Appl. Phys. **57**, 249 (1985).

[89] G. Bai and M. A. Nicolet, J. Appl. Phys. **70**, 649 (1991).

[90] M. Bianconi, E. Albertazzi, S. Balboni, L. Colombo, G. Lulli, and A. Satta, Nucl. Instrum. Methods Phys. Res., Sect. B **230**, 185 (2005).